RSC Advances

PAPER

View Article Online
View Journal | View Issue

Cite this: *RSC Adv.*, 2024, **14**, 21938

Highly dispersed noble metal nanoparticle composites on biomass-derived carbon-based carriers: synthesis, characterization, and catalytic applications†

Ya-Xin Ji,‡[a] Wei Li,‡[b] Ya-Xi Wu,[a] Xue-Fei Zhou,[a] Lin Bao*[a] and Wen-Yan Zhang *[a]

Precious metal nanoparticles have been widely investigated due to their excellent activity shown in catalysis and sensing. However, how to prepare highly dispersed noble metal nanoparticles to improve the lifetime of catalysts and reduce the cost is still an urgent problem to be solved. In this study, a carbon-based carrier material was prepared by an expansion method and loaded with Pd or Ag nanoparticles on this carbon material to synthesize precious metal nanoparticle composites, which were characterized in detail. The results show that the nanoparticles prepared using this method exhibit superior dispersion. Under the synergistic effect of noble metal nanoparticles and porous carbon carriers, the composites exhibited excellent catalytic degradation of *p*-nitrophenol and showed excellent sensing performance in the modified hydrogen peroxide sensor electrode. This approach is highly informative for the preparation of nanocomposites in medical and environmental fields.

Received 29th May 2024
Accepted 27th June 2024

DOI: 10.1039/d4ra03971h

rsc.li/rsc-advances

1. Introduction

In recent years, the excessive use of traditional fossil energy sources has triggered a series of environmental[1] and human health problems. Among them, pollutants discharged from industrial processes have polluted water bodies, posing a serious threat to water ecosystems and human health. Hydrogen peroxide adversely affects water organisms and disrupts the balance of the ecosystem. The development of efficient and reliable sensors capable of detecting hydrogen peroxide concentrations in water is crucial.[2,3] Nitroaromatic compounds are frequently present in industrial wastewater, especially in discharges from chemical plants and pharmaceutical industries. These compounds are considered toxic and persistent in the environment. They pose a significant risk to aquatic organisms and human health.[4,5] To counter the adverse effects of these compounds, the development of efficient catalysts capable of effectively detecting and degrading hydrogen peroxide and nitroaromatic compounds is essential for effective water treatment.

The noble metal nanoparticles with good biocompatibility, electrical conductivity and catalytic properties play a particularly important role in the catalytic degradation reduction of 4-nitrophenol[6–8] and the electrochemical detection of hydrogen peroxide,[9–11] and have a wide range of applications in the fields of environmental science, antimicrobial materials and biomedicine. However, in their application, precious metal nanoparticles are prone to problems such as agglomeration deactivation, which reduces their usability.[12–14] Therefore, it is important to improve the dispersion of noble metal nanoparticles on the carrier.[15–18]

Usually, biomass sources are widely available to generate porous carbon as a carrier. However, the catalytic and electrochemical activities of carbon materials are lower than those of metal-based catalysts, which are not as stable as carbon materials, so porous carbon materials can be combined which can provide a substantial increase in catalytic activity[19,20] and stability.[21]

In this study, we propose a novel approach to prepare carbon-based carrier composites and load them with precious metal palladium or silver nanoparticles. Successfully achieved uniform loading of Pd nanoparticles or Ag nanoparticles on p-C by the expansion method using glucose as the carbon source in a new and improved "black bread" experiment. This ensures the green and environmentally friendly nature of the process in this experiment compared to the classical "black bread" experiment. The results showed that the Ag/p-C modified working electrode exhibited excellent sensing performance in the hydrogen peroxide sensor and the Pd/p-C showed better catalytic performance in the catalytic reduction of 4-nitrophenol. In addition, the Ag/p-C nanocomposite modified working electrode showed excellent sensing performance when applied to the hydrogen

[a]*Key Laboratory of Synthetic and Natural Functional Molecule of the Ministry of Education, Shaanxi Key Laboratory of Physico-Inorganic Chemistry, College of Chemistry & Materials Science, Northwest University, Xi'an 710127, P. R. China. E-mail: zhangwy@nwu.edu.cn*

[b]*Sino-Platinum Electronic Materials (Yunnan) Co., Ltd, Kunming 650503, China*

† Electronic supplementary information (ESI) available: Additional PXRD patterns, FT-IR, XPS, SEM, EDS. See DOI: https://doi.org/10.1039/d4ra03971h

‡ These authors contributed equally to this work.

peroxide sensor. This work provides a new synthesis route for highly dispersed and synergistic catalytic and sensing noble metal@porous carbon composite materials. It offers a new approach for the recognition and catalytic degradation of hydrogen peroxide and nitroaromatic compounds.

2. Experimental

2.1 Materials and general methods

Silver nitrate (≥99.8%) was purchased from Shanghai BiDe Pharmaceutical Technology Co. Glucose ($C_6H_{12}O_6$, 90%), 4-nitrophenol (99%), sodium borohydride ($NaBH_4$, 90%), and sodium hydroxide (NaOH, 99%) were obtained from Komeo Chemical Reagent Co. Hydrogen peroxide (H_2O_2, 99%) and phosphate buffer solution (PBS) were purchased from Oberkai. All reagents were analytical grade and used without further purification.

The micro-morphology and chemical structure of the composite were examined using a scanning electron microscope (SEM, SU8010, Japan) and transmission electron microscopy (TEM, JEM-2100F, JEOL). XRD patterns were collected on a Bruker D8 instrument. Chemical element composition distribution was analyzed using photoelectron spectroscopy (PHI5000 Versa Probe III XPS, Germany) and energy dispersive spectroscopy (EDS). The crystal was determined by X-ray diffraction (XRD, Bruker D8 ADVANCE, Germany).

The electrochemical performance was tested on a CHI760 electrochemical workstation (Shanghai CH Instrument Co., Ltd, China) with a traditional three-electrode system in PBS (pH 7.0), with glassy carbon electrodes (GCEs, 3 mm in diameter) used as working electrodes, saturated calomel electrode used as a reference electrode and platinum used as an auxiliary electrode. All electrochemical experiments were performed at room temperature (25 ± 2 °C).

2.2 Synthesis of Pd/p-C and Ag/p-C nanocomposites

20 g of glucose and 0.03 g of $PdCl_2$ were added into 20 mL of concentrated H_2SO_4 for reaction with constant stirring of the glass rod to obtain the carbonized precursor material. Added a portion of carbonized material to NaOH solution and stirred vigorously. After 12 hours of settling, wash the mixture with deionized water and dry it for 12 hours at 80 °C. This was followed by heating to 800 °C within a N_2 environment at a rate of 5 °C min^{-1} and then annealing for 3 hours to produce Pd/p-C nanocomposite material.

The preparation method of Ag/p-C nanocomposites is similar to that of Pd/p-C nanocomposites, with the exception that palladium chloride is substituted with silver nitrate, and the calcination temperature was changed to 500 °C.

2.3 Preparation of H_2O_2 non-enzymatic electrochemical sensor electrode

The experimentally prepared nanocomposite dispersion (1 mg mL^{-1}) was dripped onto the surface of the polished glassy carbon electrode, and after drying naturally in the air, 5 μL of 1% mass fraction naphthol solution was dripped onto the modified electrode, which was dried naturally at room temperature, to obtain the working electrode, and the p-C electrode was prepared for comparison, and finally, a series of electrode slices were obtained as the electrode specimens used for electrochemical tests.

2.4 The catalytic reduction of 4-NP

In a typical experiment of 4-NP reduction: 0.5 mL of 4-NP solution (1 mmol L^{-1}) and 50 μg of catalyst were dissolved in water and loaded into a cuvette at the same time, followed by the addition of 0.1 mL of freshly prepared $NaBH_4$ solution (1 mol L^{-1}) to complete the preparation of the catalytic test solution.

3. Result and discussion

3.1 Characterization of Pd/p-C and Ag/p-C nanocomposites

After loading the metal particles, it can be noticed that the characteristic diffraction peaks of glucose disappear and a broad diffraction peak representing the amorphous carbon substrate in the amorphous state appears at around 26°, indicating the successful carbonization of glucose. The Pd/p-C nanocomposites have significant diffraction peaks at 2θ = 40.1°, 46.7°, 68.1°, 82.1°, and 86.6° (Fig. 1a). These diffraction peaks correspond to the face-centered cubic structure crystal planes (111), (200), (220), (311), and (222) of the palladium monomers,[22] which indicates that the Pd ions have been successfully reduced to palladium nanoparticles. At the same time, it can be found that there are also very weak diffraction peaks representing the palladium compounds, which is possible because a small portion of the palladium ions have not been combined with OH^-, and are still present in the form of the metal compounds. Similarly the five distinct diffraction peaks of Ag/p-C nanocomposites at 2θ = 38.1°, 44.2°, 64.3°, 77.3°, and 81.4° are consistent with the crystallographic surfaces (111), (200), (220), (311), and (222) occurring in the face-centered cubic structure of metallic Ag.[23] The results showed that all Ag ions were successfully reduced to silver nanoparticles (Ag NPs) with good crystallinity.

The FT-IR spectrum of glucose (Fig. 1b) shows a broad and strong peak at 3300 cm^{-1} representing the hydroxyl (–OH)

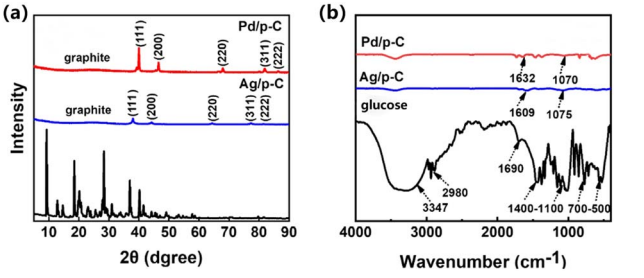

Fig. 1 (a) XRD spectrum of glucose and Ag/p-C, Pd/p-C nanocomposites; (b) IR spectrum of glucose and Ag/p-C, Pd/p-C nanocomposites.

stretching vibration,[15,24] the C–H stretching vibration peaks are a few moderately weak peaks at 2980 cm^{-1},[25] and the aldehyde peaks (–CHO) are at around 1650 cm^{-1}, and several peaks with cleavage around 1400 cm^{-1}–1100 cm^{-1} can be observed. This represents the C–O stretching vibrational peaks, the bending vibrational peaks of the marginal carbon C–H appeared around 930 cm^{-1}, and the peaks at 700 cm^{-1}–500 cm^{-1} corresponded to the ring respiration vibrational peaks, which are functional groups corresponding to glucose. In comparison, it can be found that compared to glucose, the FT-IR spectra of Ag/p-C and Pd/p-C nanocomposites show very weak peaks of –OH, C=O, and C–O, which may be some irregular bonds remaining at the edge of the amorphous carbon substrate, and show obvious C=C and C–C bonds, which constitute the main body of the carbon skeleton, with vibrational peaks appearing at 1626 cm^{-1} and 1070 cm^{-1} around.[26,27] The physical properties of porous carbon nanocomposites, such as the distribution, size and nature of the nanoparticles, as well as the accessible surface area and pore structure of the carbon substrate, are the main influences on the properties of the composites.[28,29] The morphology and structure of Pd/p-C and Ag/p-C nanocomposite materials were investigated by scanning electron microscopy (SEM). As shown in Fig. 2b, S10 and S11,† the average particle sizes of Pd NPs and Ag NPs are 10–40 nm, which are more uniformly distributed on the surfaces of the carbon substrates without obvious aggregation. The porous carbon formed a dense porous structure due to the expansion of a large amount of gas produced by the carbonization and dehydration of glucose. Secondly, as shown in Fig. 2a and d, the three-dimensional (3D) macroporous structure of the carbon skeleton of the nanocomposite with a pore size of 50–500 nm can be observed in the scanning electron microscope images. And the High-Resolution Transmission Electron Microscope (HRTEM) images (Fig. 2b and e) showed oriented and ordered lattice stripes of Pd NPs and Ag NPs, with a lattice spacing of 0.2249 nm corresponding to the Pd(111) crystal plane,[30] and lattice spacing of 0.2442 nm and 0.2156 nm corresponding to the Ag(111) and Ag(200) crystal planes, respectively.[31] In addition, the Energy Dispersive Spectrometer (EDS) (Fig. S1 and S2†) and mapping patterns (Fig. 2c and f) indicate the presence of C, O, and Pd/Ag elements, and the mapping patterns (Fig. 2c and f) show that the whole carbon substrate is completely covered by Pd NPs and Ag NPs, and the Pd NPs and Ag NPs are successfully

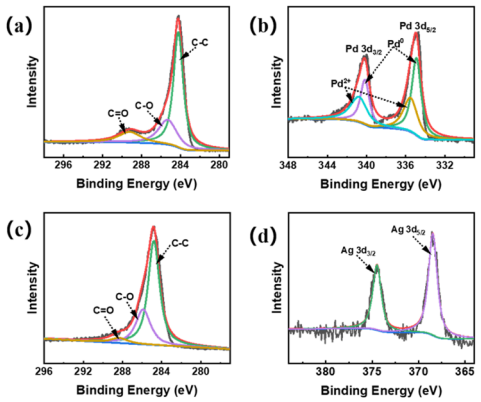

Fig. 3 XPS profiles of Pd/p-C nanocomposites: (a) C 1s; (b) Pd 3d; XPS profiles of Ag/p-C nanocomposites: (c) C 1s; (d) Ag 3d.

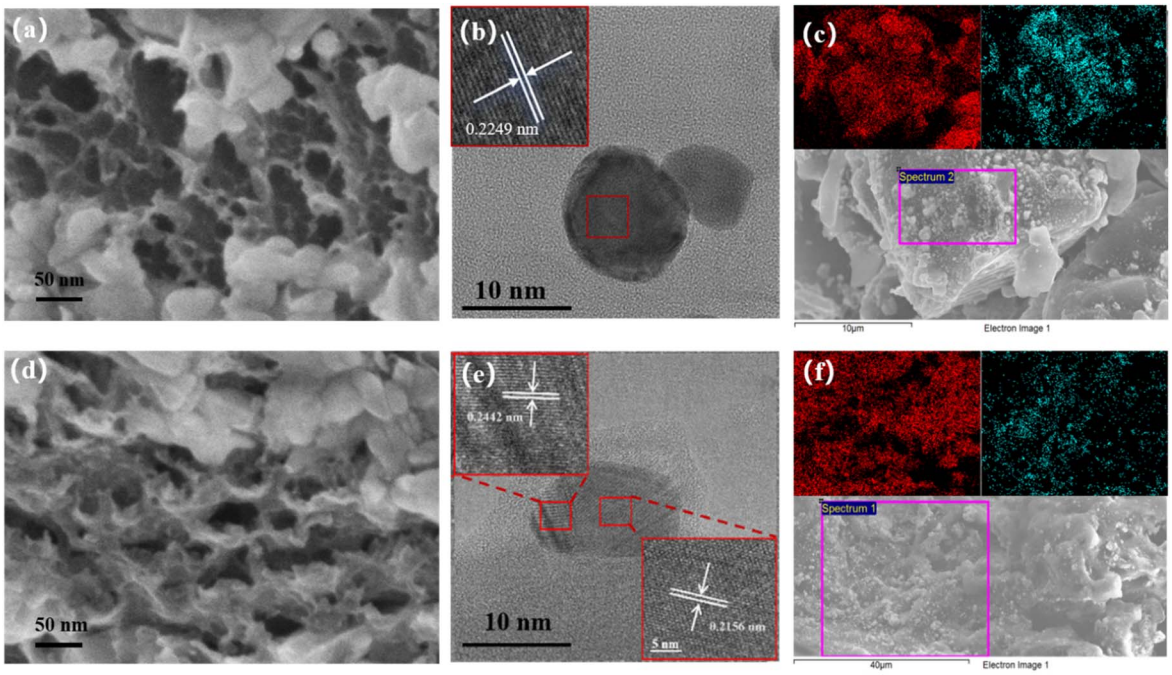

Fig. 2 (a) SEM images for the Pd/p-C nanocomposites; (b) HRTEM images for the Pd/p-C nanocomposites; (c) EDS and elemental mapping of Pd/p-C nanocomposites (red: C; blue: Pd); (d) SEM images for the Ag/p-C nanocomposites; (e) HRTEM images for the Ag/p-C nanocomposites(f) EDS and elemental mapping of Ag/p-C nanocomposites(red: C; blue: Ag).

loaded onto the carbon substrate with a relatively uniform distribution. The BET surface area of Ag/p-C was proved to be 864.8138 m^2 g^{-1} by N_2 adsorption and desorption curves (Fig. S14†).

To investigate the decoration mechanism of Pd nanoparticles and Ag nanoparticles on carbon substrates, the chemical states of the elements were analyzed by X-ray photoelectron spectroscopy (XPS). The full spectrum (Fig. S3†) shows the presence of major C 1s, O 1s, and Pd 3d peaks, and three peaks of C 1s at 284.7 eV, 286.6 eV, and 289.9 eV in Fig. 3a, which are attributed to C–C, C–O, and C═O bonds, respectively. In addition, the XPS spectrum of O 1s in Fig. S4† has three peaks at 532.1 eV (C═O), 533.9 eV (C–O), and 537.0 eV (–OH), which corresponds to certain irregular bonds remaining on the amorphous carbon rim carbon in the amorphous state.[32] In the Fig. 3b it can be observed that there are two peaks located at 335.6 eV and 340.7 eV which correspond to the $3d_{5/2}$ orbitals and $3d_{3/2}$ orbitals of the metallic palladium monomers indicating the presence of Pd at zero valence which reveals that the palladium ions have been successfully thermally reduced. It can also be seen that there are two small peaks at 337.4 eV and 342.7 eV, which correspond to the $3d_{5/2}$ and $3d_{3/2}$ orbitals of Pd^{2+},[33] indicating that a very small amount of palladium ions in the corresponds to the XRD results as well. XPS results of Ag/p-C were also analysed. The full spectrum (Fig. S5†) shows the presence of major C 1s, O 1s, and Ag 3d peaks. The two distinct peaks are located at the binding energies of 367.9 eV and 373.9 eV, which correspond to the $3d_{5/2}$ and $3d_{3/2}$ orbitals of the metal Ag0,[34] indicating that the silver exists at zero valence, which proves that the silver ions have been successfully reduced completely by thermal reduction, as shown in Fig. 3d.

3.2 Catalytic reduction of 4-NP

The catalytic reduction reaction of 4-NP catalyzed degradation to 4-AP with $NaBH_4$ as the reducing agent was used as a model system to investigate the catalytic performance of the catalyst. When the ready-made $NaBH_4$ solution was added, the absorption peak was red-shifted from 317 nm to 400 nm due to the conversion of 4-NP to 4-NP anion (Fig. S6†). The peak value of the absorption peak of 4-NP remained almost unchanged without the addition of the catalyst at room temperature, and remained essentially unchanged even when the reaction time was further extended, suggesting that in the presence of only $NaBH_4$ alone 4-NP could not be reduced to 4-AP (Fig. 4a). When the carbon substrate was used as a catalyst (Fig. S7†), the peak of 4-NP also remained almost unchanged within 1 h and no absorption peak representing 4-AP was produced at 317 nm, indicating that the pure carbon substrate was not catalytically active for this reaction system. In addition, it can be obtained through Fig. 4b and c. Pd/p-C and Ag/p-C catalysts enhanced the reduction rate and completed the catalytic reduction of 4-NP within 400 s and 540 s, respectively.

The rate constant of the catalytic reaction is still evaluated here by using the formula $k_t = -\ln(c_t/c_0) = -\ln(A_t/A_0)$ for the first-order rate constant k, where A_t and A_0 represent the absorbance value at a certain moment and the initial absorbance value, respectively.[35] The linear plot of $-\ln(A_t/A_0)$ *versus* reaction time under the same conditions (Fig. 4d) allows a clear comparison of the catalytic performance of the investigated catalysts. Moreover, the rate constant $k = 6.3 \times 10^{-3}$ s^{-1} of Pd/p-C catalyst is not only better than that of Ag/p-C catalyst but also the catalytic performance is better than that of some other

Table 1 Performance comparison of several typical H_2O_2 sensors

Catalyzer	Catalytic rate (s^{-1})	Ref.
Cu-OMS-2	0.3×10^{-3}	36
Au NPs	6.0×10^{-3}	37
Au/GO NPs	6.13×10^{-3}	38
Ag/GO NPs	3.47×10^{-3}	39
Pd–graphene nanohybrids	3.28×10^{-3}	40
Ag/p-C	5.15×10^{-3}	This work
Pd/p-C	6.3×10^{-3}	This work

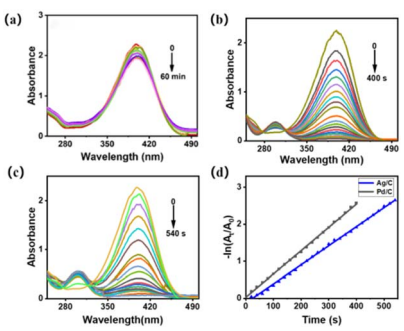

Fig. 4 (a) UV-vis plots of catalytic reduction of 4-NP by catalyst carbon (b) UV-vis plots of catalytic reduction of 4-NP by catalyst Pd/p-C, (c) UV-vis plots of catalytic reduction of 4-NP by catalyst Ag/p-C Pd/p-C; (d) plots of catalytic time *versus* $-\ln(A_t/A_0)$ with Pd/p-C and Ag/p-C as catalysts.

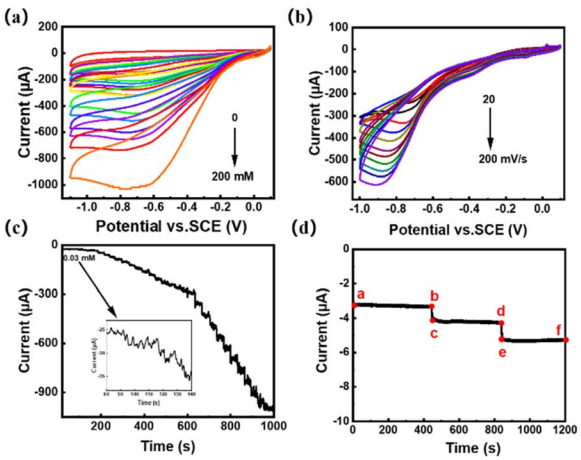

Fig. 5 (a) CV curves of different H_2O_2 (0–200 mM) concentrations at a scanning rate of 50 mV s^{-1}; (b) CV curves measured at different H_2O_2 concentrations of 50 mM with the CV curves measured at scanning rates (20–200 mV s^{-1}); (c) amperometric response of Ag/p-C electrodes with continuous addition of H_2O_2; (d) amperometric response of Ag/p-C electrodes to the addition of different analytes.

Table 2 Performance comparison of several typical H_2O_2 sensors

Sensors	Linear range (mM)	Sensitivity (μA mM^{-1} cm^{-2})	Detection limit (nM)	Ref.
CμF/Ag NPs-Naf	0.10–80.00	—	480	43
Ag/NCNFs	0.02–20	142.2	150	44
Ag-rGO	0.01–43	0.0262	4800	45
AgNPs-NCNTs	0.001–11	1004.9	30	46
AgNPs	—	0.0481	110	47
Ag-MnOOH-GO/GCE	0.0005–17.8	59.1	200	48
GO-Fe_3O_4-PAMAM-Pd/GCE	0.05–160	5.22	10	49
$AgNPs^{L\text{-}Pro}$/GC	0.0001–5.145	12.60	50	50
AgNPs/NCNFs	0.02–20	142.2	150	51
Nf/Pd@rGO-APTES/GCE	0.0007–13.5	1164.3	210	52
MOF/MWCNT	0.001–8.159	157	700	53
BG-AgNW	0.01–25	338.1	310	54
CuO-rGO	0.05–532	57.6	4.3	55
Cs/α-MnO_2/GCE	0.00024–0.1, 0.1–6.67	550	80	56
Ag/p-C	0.0003–1.3	127.58	8.37	This work

nanocomposites, as compared in Table 1. The excellent performance of the Pd/p-C nanocomposites is mainly attributed to the synergistic effect of the nanoparticles and porous carbon carriers. Pd nanoparticles exhibit higher catalytic activity than Ag nanoparticles. Additionally, the use of porous carbon with a high porosity rate prevents the aggregation of metal nanoparticles. This synergistic combination provides more active sites for reactants, thereby enhancing catalytic performance.

3.3 Electrochemical performance testing

Carbon nanotube composites provide a good platform for the detection of H_2O_2 sensors since they possess small size, large specific surface area, active sites, chemical stability and good electrical conductivity.[41] The electrochemical characterization was done with the three-electrode setup, tested in 0.1 mol L^{-1} pH = 7.0 PBS, and initially voltammetric analysis between −1.2 and 0 V. Using a 50 mV s^{-1} scan rate. Fig. 5a shows the cyclic voltammetry analysis of the Ag/p-C electrode at different H_2O_2 concentrations at a sweep rate of 50 mV s^{-1}. It can be found that the peak value of the reduction current peak increases with the increase of H_2O_2 concentration, as shown by the linear fitting plot of the peak current of Ag/p-C electrode *versus* H_2O_2 concentration in Fig. S9† and there is a quite good linear relationship between the peak current of H_2O_2 and the concentration of H_2O_2 in the concentration range of 0–200 mmol L^{-1} (R^2 = 0.999). Fig. 5b shows the cyclic voltammetry analysis performed at different scan rates at the H_2O_2 concentration of 50 mM. As shown in Fig. S8,† the peak value of the reduction current peak increases progressively with the increase of the sweep rate (20–200 mV s^{-1}) and there is a good linear relationship between the peak current and the square root of the sweep rate (R^2 = 0.998). Compliance with the Randles–Sevcik equation $i_p = 0.4463n^{3/2}F^{3/2}AD_{app}{}^{1/2}Cv^{1/2}/(RT)^{1/2}$ reveals the controllable character of the diffusion process.[42]

The amperometric response plots of the Ag/p-C electrode over time at different H_2O_2 concentrations at a potential of −0.6 V (Fig. 5c) showed that the constructed electrochemical sensor showed a good linear relationship ($R^2 = 0.999$) within the current range of 3.0×10^{-7} to 1.3×10^{-3} mol L^{-1} (Fig. S9†). Based on linear fitting, the sensitivity was calculated to be 127.58 μA mM^{-1} cm^{-2}, and the detection limit was 8.37×10^{-9} mol L^{-1} (S/N = 3). The comparison in Table 2 shows that the wide linear range, low detection limit and high sensitivity of the electrode can be attributed to the excellent synergistic effect between Ag NPs and porous carbon substrate.

Finally, the anti-interference performance of the Ag/p-C electrode was evaluated by chronoamperometric analysis. Three electroactive substances (ascorbic acid (AA), uric acid (UA), and glucose (Glu)) were measured simultaneously at −0.6 V in 0.1 mol per L PBS with 5 mmol per L H_2O_2 *versus* 10 mmol L^{-1}. The response of ascorbic acid (AA), uric acid (UA), and glucose (Glu) are shown in the ab, cd, and ef segments in Fig. 5. It can be seen that the injections of three electroactive substances caused a negligible response, whereas the injection of H_2O_2 showed a large response as can be seen by the bc and de segments. Indicating the Ag/p-C electrode had good anti-interference properties.

4. Conclusion

In this work, a thermal expansion method was successfully explored to synthesize Pd/p-C and Ag/p-C nanocomposites, ensuring the environmentally friendly nature of the experimental process. The resultant nanoparticles exhibited higher dispersion compared to alternative synthesis methods. The catalytic reduction of 4-nitrophenol by Ag/p-C nanocomposites exhibited excellent catalytic performance with a rate constant of $k = 6.3 \times 10^{-3}$ s^{-1}; the working electrode modified with Ag/p-C nanocomposites was applied to the hydrogen peroxide sensor to exhibit excellent sensing performance, which showed a wide range of 3.0×10^{-7} mol L^{-1} to 1.3×10^{-3} mol L^{-1} range, a wide linear range, a good sensitivity of 127.58 μA mM^{-1} cm^{-2}, and a low detection limit of 8.37×10^{-9} mol L^{-1} (S/N = 3), which makes the preparation of nanocomposites in medical, environmental and other fields of strong reference value.

Data availability

The authors confirm that the data supporting the findings of this study are available within the article and its ESI.† Additional data that support the findings of this study are available on request from the corresponding author.

Conflicts of interest

The authors declare no competing financial interests.

Acknowledgements

We are grateful for the financial support provided by the the Science and Technology projects of Yunnan Precious Metals Laboratory, Grant Number YPML-2023050206, the Shaanxi Science and Technology Department (2022GY-384, 2022JBGS2-07, 2021LLRH-05-21, 2022QFY06-06).

Notes and references

1 R. J. Van Putten, J. C. Van der Waal and E. De Jong, Hydroxymethylfurfural, A versatile platform chemical made from renewable resources, *Chem. Rev.*, 2013, **113**, 1499–1597.
2 D. L. Pardieck, E. J. Bouwer and A. T. Stone, Hydrogen peroxide use to increase oxidant capacity for in situ bioremediation of contaminated soils and aquifers: A review, *J. Contam. Hydrol.*, 1992, **9**, 221–242.
3 C. J. Tredwin, S. Naik and N. J. Lewis, Hydrogen peroxide tooth-whitening (bleaching) products: Review of adverse effects and safety issues, *Br. Dent. J.*, 2006, **200**, 371–376.
4 J. Liang, Z. Liang and R. Zou, Heterogeneous Catalysis in Zeolites, Mesoporous Silica, and Metal-Organic Frameworks, *Adv. Mater.*, 2017, **29**, 1701139.
5 Q. Wu, A. Y. Li and R. B. He, Enhancement of catalytic activity for hydrogenation of nitroaromatic by anionic metal-organic framework, *Chin. Chem. Lett.*, 2023, **35**, 108639.
6 X. W. Han, S. Guo and T. Li, Construction of Ag/3D-reduced graphene oxide nanocomposite with advanced catalytic capacity for 4-nitrophenol and methylene blue, *Colloids Surf., A*, 2022, **650**, 128688–128697.
7 W. M. S. Abdel, M. M. Hefny and E. S. Abd, Removal of chemical and microbial water pollutants by cold plasma combined with Ag/TiO_2-rGO nanoparticles, *Sci. Rep.*, 2022, **12**, 9850–9875.
8 B. Mahanta, H. Al Mamun and M. Konwar, Non-Enzymatic Electrochemical Biosensor for Dopamine Detection Using MoS_2/rGO/Ag Nanostructure, *ChemistrySelect*, 2023, **8**, e202205030–e202205045.
9 Q. Z. Fan, L. Lin and Z. L. Jian, Biomass-derived carbon fibers modified by Ag/rGO for high-performance Li metal composite anode, *J. Mater. Sci.: Mater. Electron.*, 2023, **34**, 10854–10868.
10 G. S. Kumbhar, S. V. Patil and P. D. Sarvalkar, Synthesis of a Ag/rGO nanocomposite using Bos taurus indicus urine for nitroarene reduction and biological activity, *RSC Adv.*, 2022, **12**, 35598–35612.
11 C. Li, C. Z. Wang and H. Y. Liu, Facile and green synthesis of clean porous Pd/2D-material nanocomposites with improved catalytic properties in 4-nitrophenol reduction reaction-the first part, *Curr. Chin. Sci.*, 2021, **1**, 252–259.
12 A. T. E. Vilian, R. C. Sang and G. Krishnan, Pd nanospheres decorated reduced graphene oxide with multi-functions: highly efficient catalytic reduction and ultrasensitive sensing of hazardous 4-nitrophenol pollutant, *J. Hazard. Mater.*, 2017, **333**, 54–62.
13 X. C. Liao, C. Y. Ma and C. L. Zhao, An immunosensor detects carcinoembryonic antigen by dual catalytic signal enhancer hydrogen peroxide based on in-situ reduction of silver nanoparticles with dopamine and graphene high-load cobalt tetroxide, *Microchem. J.*, 2020, **160**, 105602–105612.
14 A. Karczmarska, M. Adamek and S. El Houbbadi, Carbon-Supported Noble-Metal Nanoparticles for Catalytic Applications—A Review, *Crystals*, 2022, **12**, 584.
15 P. H. Yan, S. B. Xi and H. Peng, Facile and eco-friendly approach to produce confined metal cluster catalysts, *J. Am. Chem. Soc.*, 2023, **145**, 9718–9728.
16 P. H. Yan, X. X. Tian and E. M. Kennedy, The role of Ni sites located in mesopores in the selectivity of anisole hydrodeoxygenation, *Catal. Sci. Technol.*, 2022, **12**, 2184–2196.
17 P. H. Yan, J. Mensah and A. Adesina, Highly-dispersed Ni on bea catalyst prepared by ion-exchange-deposition-precipitation for improved hydrodeoxygenation activity - science direct, *Appl. Catal., B*, 2020, **267**, 118690.
18 P. H. Yan, E. M. Kennedy and H. M. Zhang, Catalytic hydropyrolysis of lignocellulosic biomass to BTX and biofuels over zeolite beta based catalysts, *Fuel*, 2023, **332**, 125946.
19 P. Pachfule, A. Acharjya and J. Roeser, Donor-acceptor covalent organic frameworks for visible light induced free radical polymerization, *Chem. Sci.*, 2019, **10**, 8316–8322.
20 Y. F. Zhu, D. Y. Zhu and Y. Chen, Porphyrin-based donor-acceptor COFs as efficient and reusable photocatalysts for PET-RAFT polymerization under broad spectrum excitation, *Chem. Sci.*, 2021, **12**, 16092–16099.
21 T. Y. Yoo, J. M. Yoo and A. K. Sinha, Direct Synthesis of Intermetallic Platinum-Alloy Nanoparticles Highly-Loaded on Carbon Supports for Efficient Electrocatalysis, *J. Am. Chem. Soc.*, 2020, **142**, 14190–14200.
22 H. W. Kroto, J. R. Heath and S. C. O′Brien, C60: Buck minster fullerene, *Nature*, 1985, **318**, 162–163.
23 D. Ugarte, Curling and closure of graphitic networks under electron-beam irradiation, *Nature*, 1992, **359**, 707–709.
24 P. H. Yan, I. N. Azreena and H. Peng, Catalytic hydropyrolysis of biomass using natural zeolite-based catalysts, *Chem. Eng. J.*, 2023, **476**, 146630.
25 P. H. Yan, X. X. Tian and E. M. Kennedy, Advanced in situ IR spectroscopy study of anisole hydrodeoxygenation over Ni/SiO2 catalysts, *J. Catal.*, 2023, **427**, 115102.

26 J. C. Serrano-Ruiz and J. A. Dumesic, Catalytic routes for the conversion of biomass into liquid hydrocarbon transportation fuels, *Energy Environ. Sci.*, 2011, **4**, 83–99.
27 P. Dürre, Biobutanol: An attractive biofuel, *Biotechnol. J.*, 2007, **2**, 1525–1534.
28 S. Gadipelli and Z. X. Guo, Graphene-based materials: synthesis and gas sorption, storage and separation, *Prog. Mater. Sci.*, 2015, **69**, 1–60.
29 H. G. Shiraz and O. Tavakoli, Investigation of graphene-based systems for hydrogen storage, *Renewable Sustainable Energy Rev.*, 2017, **74**, 104–109.
30 H. C. A. Murthy, T. D. Zeleke and C. R. Ravikumar, Electrochemical properties of biogenic silver nanoparticles synthesized using Hagenia abyssinica (Brace) JF. Gmel. medicinal plant leaf extract, *Mater. Res. Express*, 2022, **7**, 055016.
31 K. Lejaeghere, V. S. Van and G. O. Van, Error estimates for solid-state density-functional theory predictions: an overview by means of the ground-state elemental crystals, *Crit. Rev. Solid State Mater. Sci.*, 2014, **39**, 1–24.
32 T. C. Ezeji, N. Qureshi and H. P. Blaschek, Bioproduction of butanol from biomass: from genes to bioreactors, *Curr. Opin. Biotechnol.*, 2007, **18**, 220–227.
33 M. M. Wang, Z. X. He and M. Chen, Aryl sulfonate anion stabilized aromatic triangular cation [Pd3]+: syntheses, structures and properties, *RSC Adv.*, 2023, **13**, 29689–29694.
34 P. Attri, S. Garg and J. K. Ratan, Silver nanoparticles from Tabernaemontana divaricate leaf extract: mechanism of action and bio-application for photo degradation of 4-aminopyridine, *Environ. Sci. Pollut. Res.*, 2022, **10**, 24856–24875.
35 A. Schirmer, M. A. Rud e and X. Li, Microbial biosynthesis of alkanes, *Science*, 2010, **329**, 559–562.
36 Y. Huang, K. Zheng and X. Liu, Optimization of Cu catalysts for nitrophenol reduction, click reaction and alkyne coupling, *Inorg. Chem. Front.*, 2020, **7**, 939–945.
37 H. Rodríguez Molina, J. L. Santos Muñoz and M. I. Domínguez Leal, Carbon supported gold nanoparticles for the catalytic reduction of 4-nitrophenol, *Front. Chem.*, 2019, **7**, 548.
38 T. Wu, L. Zhang and J. Gao, Fabrication of graphene oxide decorated with Au–Ag alloy nanoparticles and its superior catalytic performance for the reduction of 4-nitrophenol, *J. Mater. Chem. A*, 2013, **1**, 7384–7390.
39 N. Berahim, W. J. Basirun and B. F. Leo, Synthesis of bimetallic gold-silver (Au-Ag) nanoparticles for the catalytic reduction of 4-nitrophenol to 4-aminophenol, *Catalysts*, 2018, **8**, 412.
40 Z. Wang, C. Xu and G. Gao, Facile synthesis of well-dispersed Pd–graphene nanohybrids and their catalytic properties in 4-nitrophenol reduction, *RSC Adv.*, 2014, **4**, 13644–13651.
41 H. Nie, Z. Yao and X. Zhou, Nonenzymatic electrochemical detection of glucose using well-distributed nickel nanoparticles on straight multi-walled carbon nanotubes, *Biosens. Bioelectron.*, 2011, **30**, 28–34.
42 B. W. L. Jang, R. Gläser and M. Dong, Fuels of the future, *Energy Environ. Sci.*, 2010, **3**, 253–259.
43 T. R. Wu, H. L. Shen and L. Sun, Facile synthesis of Ag interlayer doped graphene by chemical vapor deposition using polystyrene as solid carbon source, *ACS Appl. Mater. Interfaces*, 2012, **4**, 2041–2047.
44 M. Gholami and B. Koivisto, A flexible and highly selective non-enzymatic H_2O_2 sensor based on silver nanoparticles embedded into Nafion, *Appl. Surf. Sci.*, 2019, **467**, 112–118.
45 H. Guan and Y. L. andZ. Bai, Ag nanoparticles embedded in N-doped carbon nanofibers: A superior electrocatalyst for hydrogen peroxide detection, *Mater. Chem. Phys.*, 2018, **213**, 335–342.
46 N. I. Ikhsan, P. Rameshkumar and N. Yusoff, Electrocatalytic reduction of hydrogen peroxide and its non-enzymatic electrochemical detection using silver nanoparticles anchored on reduced graphene oxide, *J. Nanosci. Nanotechnol.*, 2019, **19**, 7054–7063.
47 J. Dou, G. Zhu and B. Hu, Wall thickness-tunable Ag NPs-NCNTs for hydrogen peroxide sensing and oxygen reduction reaction, *Electrochim. Acta*, 2019, **306**, 466–476.
48 B. H. Jeon, D. H. Yang and Y. D. Kim, Fabrication of silver nanoparticles in titanium dioxide/poly (vinyl alcohol) alternate thin films: A nonenzymatic hydrogen peroxide sensor application, *Electrochim. Acta*, 2018, **292**, 749–758.
49 W. Bai, F. Nie and J. Zheng, Novel silver nanoparticle-manganese oxyhydroxide-graphene oxide nanocomposite prepared by modified silver mirror reaction and its application for electrochemical sensing, *ACS Appl. Mater. Interfaces*, 2014, **6**, 5439–5449.
50 H. Alinezhad, M. Tarahomi and M. Fayazi, A non-enzymatic hydrogen peroxide sensor based on dendrimer functionalized magnetic graphene oxide decorated with palladium nanoparticles, *Appl. Surf. Sci.*, 2019, **478**, 87–93.
51 F. Zhao, M. Zhou and L. Wang, One-step voltammetric deposition of xz-proline assisted silver nanoparticles modified glassy carbon electrode for electrochemical detection of hydrogen peroxide, *J. Electroanal. Chem.*, 2019, **833**, 205–212.
52 M. Guler and Y. Dilmac, Palladium nanoparticles decorated (3-aminopropyl) triethoxysilane functionalized reduced graphene oxide for electrochemical determination of glucose and hydrogen peroxide, *J. Electroanal. Chem.*, 2019, **834**, 49–55.
53 S. Huang, L. Luo and Y. Zhou, Ultrathin two-dimension metal-organic framework nanosheets/multi-walled carbon nanotube composite films for the electrochemical detection of H_2O_2, *J. Electroanal. Chem.*, 2019, **835**, 178–185.
54 A. K. Nair, N. K. M. Sukumaran and S. Thomas, Synthesis of silver nanospheres, nanocubes, and nanowires over boron-doped graphene sheets for surface-enhanced Raman scattering application and enzyme-free detection of hydrogen peroxide, *Langmuir*, 2018, **34**, 13603–13614.
55 S. Kumar, S. Ghosh and N. C. Murmu, Electrochemical detection of H_2O_2 using copper oxide-reduced graphene oxide heterostructure, *J. Nanosci. Nanotechnol.*, 2019, **19**, 5295–5302.
56 H. Zhao, X. Zhang and Y. Xu, A hollow urchin-like α-MnO_2 as an electrochemical sensor for hydrogen peroxide and dopamine with high selectivity and sensitivity, *Microchim. Acta*, 2019, **186**, 10–218.